







Article

# Reaction Mechanism Development for Methane Steam Reforming on a Ni/Al<sub>2</sub>O<sub>3</sub> Catalyst

Jana Richter <sup>1,\*</sup>, Fabian Rachow <sup>2</sup>, Johannes Israel <sup>2</sup>, Norbert Roth <sup>1</sup>, Evgenia Charlafti <sup>2</sup>, Vivien Günther <sup>3</sup>, Jan Ingo Flege <sup>2</sup> and Fabian Mauss <sup>1</sup>

<sup>1</sup> Department of Thermodynamics/Thermal Process Engineering, Brandenburg University of Technology Cottbus—Senftenberg, Siemens-Halske-Ring 8, D-03046 Cottbus, Germany; norbert.roth@b-tu.de (N.R.); maussf@b-tu.de (F.M.)

<sup>2</sup> Department of Applied Physics and Semiconductor Spectroscopy, Brandenburg University of Technology Cottbus—Senftenberg, K.-Zuse-Straße 1, D-03046 Cottbus, Germany; rachofab@b-tu.de (F.R.); israel@b-tu.de (J.I.); charlaft@b-tu.de (E.C.); flege@b-tu.de (J.I.F.)

<sup>3</sup> LOGE Deutschland GmbH, Querstraße 48, 03044 Cottbus, Germany; vivien.guenther@logesoft.com

\* Correspondence: jana.richter@b-tu.de

**Abstract:** In this work, a reliable kinetic reaction mechanism was revised to accurately reproduce the detailed reaction paths of steam reforming of methane over a Ni/Al<sub>2</sub>O<sub>3</sub> catalyst. A steady-state fixed-bed reactor experiment and a 1D reactor catalyst model were utilized for this task. The distinctive feature of this experiment is the possibility to measure the axially resolved temperature profile of the catalyst bed, which makes the reaction kinetics inside the reactor visible. This allows for understanding the actual influence of the reaction kinetics on the system; while pure gas concentration measurements at the catalytic reactor outlet show near-equilibrium conditions, the inhere presented temperature profile shows that it is insufficient to base a reaction mechanism development on close equilibrium data. The new experimental data allow for achieving much higher quality in the modeling efforts. Additionally, by carefully controlling the available active surface via dilution in the experiment, it was possible to slow down the catalyst conversion rate, which helped during the adjustment of the reaction kinetics. To assess the accuracy of the revised mechanism, a monolith experiment from the literature was simulated. The results show that the fitted reaction mechanism was able to accurately predict the experimental outcomes for various inlet mass flows, temperatures, and steam-to-carbon ratios.

**Keywords:** kinetic reaction mechanism development; 1D modeling; reaction rates; methane steam reforming; fixed-bed reactor experiments; nickel catalyst



**Citation:** Richter, J.; Rachow, F.; Israel, J.; Roth, N.; Charlafti, E.; Günther, V.; Flege, J.I.; Mauss, F. Reaction Mechanism Development for Methane Steam Reforming on a Ni/Al<sub>2</sub>O<sub>3</sub> Catalyst. *Catalysts* **2023**, *13*, 884. <https://doi.org/10.3390/catal13050884>

Academic Editors: Bin Xu and Yu Gong

Received: 29 March 2023

Revised: 4 May 2023

Accepted: 5 May 2023

Published: 13 May 2023



**Copyright:** © 2023 by the authors. Licensee MDPI, Basel, Switzerland. This article is an open access article distributed under the terms and conditions of the Creative Commons Attribution (CC BY) license (<https://creativecommons.org/licenses/by/4.0/>).

## 1. Introduction

Hydrogen has been part of the debate on climate change for several years and is, more than ever, in the political spotlight as it has the potential to play a major role in the transition to a low-carbon economy and help reduce greenhouse gas emissions [1]. There is a whole raft of arguments that underline the advantages of hydrogen. It is an energy source without local pollution, and it is the most abundant element in the universe. Hydrogen further has the highest energy per unit mass and can be directly converted into thermal, mechanical and electrical energy [2]. In addition to its use as an energy carrier, hydrogen also serves as basic material for the chemical industry, such as ammonia synthesis using the Haber–Bosch process [3]. Thus, the European Union actively supports the installation of a hydrogen-based energy system as a pillar to achieve the transition to new energy sources and meet the goals of the European Green Deal [4,5]. Hydrogen as a fuel, in different kinds of fuel cells, has also been gaining relevance during the last decades [6,7]. Among others, there are innovative approaches, as presented in [8], for decentralized energy productions, wherein hydrogen gained from methane steam reforming (MSR) is used in a MGT-SOFC hybrid

system consisting of a recuperated micro gas turbine (MGT) process with an embedded solid oxide fuel cell (SOFC) subsystem.

Next to MSR, hydrogen can be produced from methane via numerous chemical reaction paths, e.g., dry reforming, partial oxidation, methane cracking, gasification of carbon, and the water–gas shift reaction [9]. Nevertheless, more than 80% of the whole hydrogen produced is made using MSR at an energy efficiency of 74–85% [10]. The steam reforming reaction itself, being strongly endothermic, converts two stable molecules into the more reactive syngas, as visible in Equation (1) [9,11]:



As MSR is highly endothermic, the large scale production of hydrogen requires a suitable, efficient, and thermally stable catalyst that enables reliable hydrogen production. In this work, a nickel-based catalyst on an alumina substrate was chosen for the MSR. Due to its low cost combined with high activity, nickel catalysts have been extensively studied in the past, and MSR catalysts have been continuously improved by advances in catalyst technologies and preparation methods [12]. Nanoscale particle synthesis methods, including impregnation, co-sputtering and chemical vapor deposition, enable highly dispersed dopants and high activity, which improves the catalysts' stability. The addition of metallic or bimetallic species to a Ni-based catalyst has been shown to improve the durability, activity, and selectivity of the catalyst and, thus, improve catalyst properties with regard to typical problems such as active oxidation, coke formation, sintering and segregation [13]. The previously listed disadvantages of Ni-based catalysts can also be avoided by the use of noble metal catalysts. Noble metal catalysts are highly active in MSR but less susceptible to oxidation deactivation and coke formation. However, economic efficiency is the limiting factor in the use of noble metal catalysts [14].

Even though efficiency, availability and economic considerations make nickel widely used for MSR, attention must be paid to the aforementioned issue of coke formation [15]. This problem needs consideration when setting the reaction conditions as this condition highly influences the coke formation tendency [16]. It is evident that the steam-to-carbon (S/C) ratio, pressure and temperature range are the main influencing parameters affecting coke formation [16]. According to [17], hydrocarbons dissociate on the metal surface to produce carbon deposits, which are either gasified (steam reforming) or encapsulate nickel and facilitate the formation of carbon whiskers to produce coke. Even if the coke formation does not necessarily entail catalyst deactivation, the pressure drop will increase and may require catalyst replacement [17].

The discussion above demonstrates that the optimization of catalyst design and the process control of MSR are indispensable. The process optimization can be supported by an accurate and efficient chemical model. The development of kinetic reaction models for catalytic reactions has a long history, dating back to the early 20th century. The pioneering work of Langmuir and Hinshelwood in the 1930s laid the foundation for the modern approach to kinetic modeling, which involves the development of a set of differential equations describing the rates of all elementary reactions involved in a catalytic process [18]. The Langmuir–Hinshelwood approach is a widely used theoretical framework for the study of heterogeneous catalysis, in which reactions occur on the surface of a solid catalyst. It describes the reaction mechanism in terms of adsorption of reaction molecules on the catalyst surface, followed by their reaction and desorption of the products [19].

The kinetic modeling was further developed in the latter half of the 20th century, with the introduction of the steady-state approximation [20] and the use of sophisticated mathematical techniques such as Monte Carlo simulations and density functional theory calculations [21]. These advances led to the development of detailed kinetic reaction models for a wide range of catalytic reactions, including steam reforming over Ni/Al<sub>2</sub>O<sub>3</sub>. Despite the progress made in the field of kinetic modeling, the development of a detailed kinetic reaction model for steam reforming over Ni/Al<sub>2</sub>O<sub>3</sub> has remained a challenge due to the complexity of the reaction mechanism. The steam reforming of hydrocarbons over

Ni/Al<sub>2</sub>O<sub>3</sub> involves multiple elementary reactions, including the adsorption, dissociation and desorption of the reactants and intermediates on the catalyst surface. The prediction accuracy of kinetic models of industrial methane steam reforming is discussed in [22]. Four different models [23–26] have been analyzed in this meta study and compared with each other. It can be concluded that the presented models describe the reformer well with relatively low deviations in relation to the experimental and literature data. However, none of the models presented in [22] provide a comprehensive mechanism for the modeling of simultaneous partial oxidation and steam reforming over nickel. This was presented for the first time in [27].

Models can be categorized into two types: phenomenological models, which capture essential features of observed rates without necessarily connecting to the chemical details of a system, and elementary-step models, which accurately describe the underlying chemical steps involved in a reaction [28]. Ref. [28] highlights the importance of elementary-step models in achieving accuracy in predicting real-world values or trends and explains that such models can be developed using either a bottom-up or top-down approach. In the context of developing chemical kinetic models, the bottom-up approach involves starting from molecular-level information and using it to obtain kinetic parameters [28]. These parameters are then used in simulations to make predictions, which can be compared to experimental observations. On the other hand, the top-down approach starts with experimental observations and uses calculations and fitting or parameter estimation to derive kinetic parameters and molecular-level information. In both approaches, the goal is to develop a model that accurately predicts the behavior of the chemical system being studied [28].

In the present work the detailed kinetic reaction model of MSR over a nickel catalyst first published by [27] is revised and verified. For this purpose, experiments were carried out in a fixed-bed reactor to obtain a comprehensive view of the reaction kinetics, as in the mentioned top-down approach, by observing the temperature along the length of the reactor and not only focusing on the nearly equilibrium reaction products. To achieve a fine resolution of the kinetics in the experiment, the catalyst bed was diluted with inert material in order to reduce the catalytic active surface.

Detailed kinetic models as developed within this work can be used in many applications, such as 1D, 2D or CFD simulations, to obtain an accurate picture of the catalytic processes. Reliable kinetic simulation models are cost-effective tools as they allow virtual process optimization and reactor design and, thus, reduce experimental time and cost. Within this paper, the computationally cost-effective 1D model, LOGEcat [29], was used to perform the simulations.

## 2. Model Description

The monolith 1D catalyst model used for the simulations in this work was presented in detail first in [30]. The model was then extended by a multi-channel model in [31] and further applied and described in [32,33]. However, for the sake of readability, this article presents detailed information about the model in this section, with emphasis on the modeling of conservation and flow equations. The model can be applied to steady-state and transient simulations. Figure 1 shows the basic concept of the model. It consists of a three-level solution with the reactor level as the frame, which includes the channel level with the possibility to simulate multiple representative channels. When running in multi-channel mode, pseudo 3D simulations are performed, taking radial heat conduction between the channels into account. As this increases the computational cost, in this paper, only single-channel simulations are considered, where radial heat transfer between the channels is not computed, but the whole catalyst is represented using one channel. At the washcoat level, the active catalytic sites are considered, and surface reactions are solved. The channel is divided into a finite number of cells with length  $\Delta x$  (see Figure 1). Due to the small catalytic channel diameter, the pressure gradients and inhomogeneities of the mixture can be neglected. Therefore, each cell can be treated as a perfectly stirred reactor

(PSR). In this work, steady-state single-channel calculations were performed. As the model only includes monolithic reactors, the physical parameters of the experimental fixed-bed reactor were chosen according to the fixed-bed reactor dimensions, and the open volume of the fixed-bed reactor was assumed to be the same as the open volume of the virtual monolithic reactor in LOGEcat [29]. The software has a sensitivity analysis tool that was applied in this work to develop the reaction mechanism, as described in detail in [34].

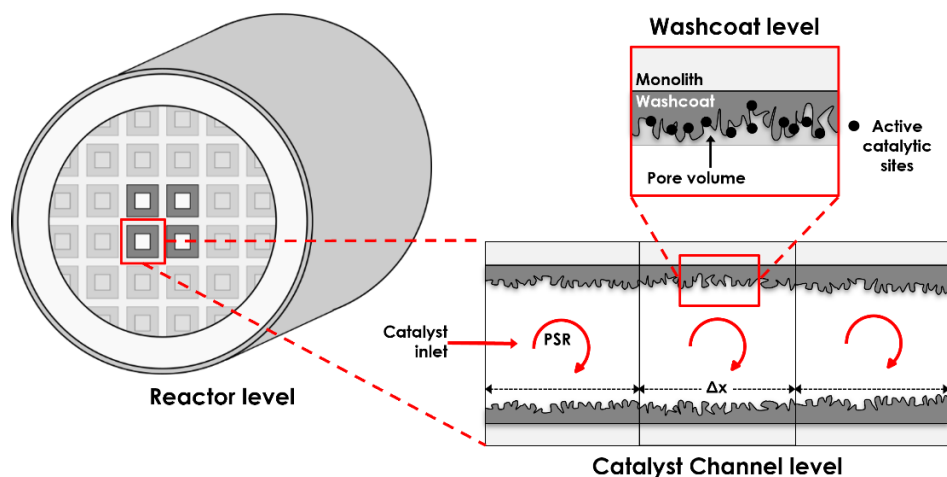


**Figure 1.** Model concept and discretization of a channel (with the cell length  $\Delta x$ ).

### 2.1. Conservation Equations

The bulk gas in each cell is modeled by a PSR, assuming constant pressure during the time step,  $\Delta t$ , in the operator splitting loop. Species transport between the bulk gas and thin-film layer is accounted for by mass transfer coefficients. The conservation equation for bulk gas species mass fractions is:

$$\begin{aligned} \rho \frac{\partial Y_{i,g}}{\partial t} = & \frac{(\rho v)_{in} A}{V_g} (Y_{i,in} - Y_{i,g}) + W_i \omega_{i,g} \\ & - \frac{P \Delta x}{V_g} W_i K_m k_{m,i} (C_{i,g} - C_{i,p}) \\ & + Y_{i,g} \frac{P \Delta x}{V_g} \sum_{j=1}^{N_g} W_j K_m k_{m,j} (C_{j,g} - C_{j,p}) \end{aligned} \quad (2)$$

where the subscript  $g$  denotes bulk gas,  $p$  gas in the thin-film layer and in the inflow from the upstream cell.  $Y_{i,g}$  is the mass fraction of species  $i$ ,  $V_g$  is the gas volume in the current cell,  $\omega_{i,g}$  is the species source term for gas phase reactions,  $K_m$  is the tuning parameter for the overall mass transfer,  $k_{m,i}$  is the convective mass transfer coefficient of species  $i$ ,  $C_{i,g}$  is the concentration of species  $i$  in the bulk gas,  $C_{i,p}$  is the concentration of species  $i$  in the thin-film layer and  $P$  is the geometric wetted perimeter of the channel. All symbols, definitions and units are explained in the Nomenclature.

The thin-film layer considers gas phase as well as surface reactions. It further includes diffusion into the pores. The conservation equation of the gas phase species is given by:

$$\begin{aligned}
 \rho_{p,l} \frac{\partial Y_{i,p,l}}{\partial t} = & \frac{P\Delta x}{V_{p,l}} W_i K_m k_{m,i} (C_{i,g} - C_{i,p,l}) \Big|_{l=1} + W_i \omega_{i,p,l} \\
 & + W_i K_e \sum_{m=1}^{N_{surf}} \frac{A_m}{V_{p,l}} \omega_{i,m} + D_i \frac{C_{i,p,l} - C_{i,p,l+1}}{w_{l+1,l}} \frac{A_m}{V_{p,l}} \\
 & - Y_{i,p,l} \sum_{j=1}^{N_g} \left[ \frac{P\Delta x}{V_{p,l}} K_m k_{m,j} W_j (C_{j,g} - C_{j,p,l}) \Big|_{l=1} \right. \\
 & \left. + W_j K_e \sum_{m=1}^{N_{surf}} \frac{A_m}{V_{p,l}} \omega_{j,m} + D_j \frac{C_{j,p,l} - C_{j,p,l+1}}{w_{l+1,l}} \frac{A_m}{V_{p,l}} \right]
 \end{aligned} \tag{3}$$

where  $V_{p,l}$  is the gas volume of the thin-film layer in washcoat layer  $l$  in the current cell;  $\omega_{i,p,l}$  is the species source term for gas phase reactions in the thin-film layer in washcoat layer  $l$ .  $N_{surf}$  is the number of different surface materials present in the catalytic converter,  $A_m$  is the catalytic surface area in the current cell;  $K_e$  is the tuning parameter for the overall reaction efficiency. An additional term for diffusion through multiple washcoat layers is accounted for by parameters  $D_i$ , which is the appropriate diffusion coefficient for species  $i$ , the subscript  $l$  is the current washcoat layer,  $w_{l+1,l}$  is the radial distance through the washcoat calculated as  $(w_{l+1} - w_l)/2$  for diffusion between washcoat layer  $l$  and  $l + 1$ . It should be noted that the source term for bulk gas species transport into the washcoat is only used for the first washcoat layer (denoted as  $|_{l=1}$ ).

The conservation equation for surface species site fractions is given by:

$$\frac{\partial \theta_{i,n}}{\partial t} = \sigma_{i,n} K_e \frac{\omega_{i,n}}{\Gamma_n} \tag{4}$$

where  $\theta_{i,n}$  is the site fraction of species  $i$  at site  $n$ ,  $\Gamma_n$  is the site density,  $\omega_{i,n}$  is the species source term from reactions at site  $n$  and  $\sigma_{i,n}$  is the site occupancy number of species  $i$  at site  $n$ .

The bulk gas energy conservation equation takes heat transport by convection and molecular transport into account. The conservation equation for the bulk gas specific enthalpy is given by:

$$\begin{aligned}
 \frac{\partial h_g}{\partial t} = & \frac{(\rho v)_{in} A}{m_g} (h_{in} - h_g) - K_h h_T \frac{P\Delta x}{m_g} (T_g - T_w) \\
 & + \frac{P\Delta x}{m_g} \sum_{j=1}^{N_g} W_j K_m k_{m,j} (C_{j,g} - C_{j,p}) (h_g - h_{j,g\leftrightarrow p})
 \end{aligned} \tag{5}$$

Here,  $h_g$  is the bulk gas specific enthalpy,  $h_T$  is the convective heat transfer coefficient between bulk gas and surface,  $T_g$  is the bulk gas temperature,  $T_w$  is the thin-film layer temperature,  $h_{in}$  is the specific enthalpy of the gas from the upstream cell and  $h_{j,g\leftrightarrow p}$  is the specific enthalpy of species  $j$  transported between the bulk gas and the thin-film layer. If the species is transported from the bulk gas, the bulk gas enthalpy is used, and if it is transported to the bulk gas, the thin-film layer enthalpy is used.

The thin-film layer temperature is assumed to be homogeneous for the substrate as well as for the gas. Furthermore, constant pressure is assumed in the thin-film layer, and kinetic energy, due to gas movement, is considered negligible. With these assumptions, the conservation equation for the surface temperature is given by:

$$\begin{aligned}
 & (\rho_s V_s c_s + \rho_p V_p c_{p,p}) \frac{\partial T_w}{\partial t} = \\
 & V_s \frac{\partial}{\partial x} \left( k_s \frac{\partial T_w}{\partial x} \right) + K_h h_T P \Delta x (T_g - T_w) \\
 & - \sum_{j=1}^{N_{g,p}} W_j P \Delta x K_m k_{m,j} (C_{j,g} - C_{j,p}) (h_{j,p} - h_{j,g \leftrightarrow p}) \\
 & - \sum_{j=1}^{N_{g,p}} W_j \left[ h_{j,p} V_p K_e \omega_{j,p} + h_{j,p} K_e \sum_{m=1}^{N_m} A_m \omega_{j,m} \right] \\
 & - K_e \sum_{m=1}^{N_m} \sum_{j=1}^{N_{s,m}} h_{j,m} W_j A_m \omega_{j,m} \\
 & + \frac{k_{s,l+1} \left( \frac{\partial T_{w,l+1}}{\partial w_{l+1,l-1}} \right) - k_{s,l-1} \left( \frac{\partial T_{w,l-1}}{\partial w_{l+1,l-1}} \right)}{w_l}
 \end{aligned} \tag{6}$$

Here,  $V_s$  is the volume of the solid wall material (washcoat and substrate) in the current cell, subscript  $s$  denotes the solid,  $c_s$  is the specific heat capacity of the solid material,  $c_{p,p}$  is the specific heat capacity in the thin-film layer at constant pressure and  $K_h$  is a tunable parameter for the heat transfer. Therefore, heat conduction along the channel, heat convection/diffusion to the bulk gas, and molecular heat transport, as well as heat released by reactions, are taken into account in this expression. An additional heat flow term is used to account for heat losses through the mat and can of the catalyst at the periphery of the substrate. Washcoat diffusion is included in the conservation equation for the surface temperature if there are multiple washcoats. The thermal conductivity of washcoat layer  $l$  is given by  $k_{s,l}$ . For single washcoats, pore diffusion is mimicked by the tuning parameter,  $K_e$ .

The heat and mass transfer coefficients,  $h_T$  and  $k_{m,i}$ , used in the conservation equations are calculated from the Nusselt and Sherwood numbers according to boundary layer theory (see, e.g., [35]). The correlations for Sherwood and Nusselt numbers, derived for simultaneously developing velocity, concentration and thermal boundary layer flows and single first-order surface reactions, presented by [36], are used:

$$Sh_i(x) = \begin{cases} \frac{0.35}{Sc_i^{1/6}} \sqrt{\frac{\left(\frac{d_h}{4}\right)^2 v}{xD_i}}, & 0 < x < \frac{\left(\frac{d_h}{4}\right)^2 v}{D_i} \left(\frac{1}{Sc_i}\right)^{1/3} \left(\frac{1.4}{Sh_{T,\infty}}\right)^2 \\ Sh_{T,\infty}, & x \geq \frac{\left(\frac{d_h}{4}\right)^2 v}{D_i} \left(\frac{1}{Sc_i}\right)^{1/3} \left(\frac{1.4}{Sh_{T,\infty}}\right)^2 \end{cases} \tag{7}$$

$$Nu(x) = \begin{cases} \frac{0.35}{Pr^{1/6}} \sqrt{\frac{\left(\frac{d_h}{4}\right)^2 v}{xD_T}}, & 0 < x < \frac{\left(\frac{d_h}{4}\right)^2 v}{D_T} \left(\frac{1}{Pr}\right)^{1/3} \left(\frac{1.4}{Nu_{T,\infty}}\right)^2 \\ Nu_{T,\infty}, & x \geq \frac{\left(\frac{d_h}{4}\right)^2 v}{D_T} \left(\frac{1}{Pr}\right)^{1/3} \left(\frac{1.4}{Nu_{T,\infty}}\right)^2 \end{cases} \tag{8}$$

where  $D_i$  is the species diffusion coefficient for species  $i$ ,  $D_T$  is the thermal diffusion coefficient and  $v$  is the fluid velocity along the channel.  $Sh_{T,\infty}$  and  $Nu_{T,\infty}$  are the asymptotic Sherwood and Nusselt numbers for constant flux boundary conditions. The values of  $Sh_{T,\infty}$  and  $Nu_{T,\infty}$  for different channel geometries are taken from [37]. In this article, the value for squared channels, 2.976, is used for both. The Schmidt number of species  $i$ ,  $Sc_i$ , is given by:

$$Sc_i = \frac{\mu_i}{\rho D_i} \tag{9}$$

Here,  $\mu_i$  is the dynamic viscosity and  $D_i$  is the diffusion coefficient of species  $i$ . The Prandtl number,  $Pr$ , is given by:

$$Pr = \frac{c_p \mu}{k_g} \quad (10)$$

Here,  $c_p$  is the heat capacity at constant pressure,  $\mu$  is the dynamic viscosity and  $k_g$  is the thermal conductivity of the gas.

## 2.2. Flow Equations

The conservation equations are defined as follows:

Mass conservation:

$$\frac{\partial(\rho)}{\partial t} + \frac{\partial(\rho v)}{\partial x} = -\frac{A_{w,G}}{m_g} \sum_{i=1}^{N_g} W_i k_{m,i} (C_{i,g} - C_{i,p}) \quad (11)$$

Momentum equation:

$$\frac{\partial(\rho v)}{\partial t} + \frac{\partial(\rho v^2)}{\partial x} + \frac{\partial p}{\partial x} = -\frac{f_F}{2} (\rho v) |v| \frac{p}{A} \quad (12)$$

where  $A$  is the cross-sectional channel area. With the assumptions of laminar and fully developed flow, the friction factor,  $f_F$ , is given by:

$$f_F = \frac{16}{Re} = \frac{16\mu}{\rho v d_h} \quad (13)$$

## 3. Experiments

### 3.1. Fixed-Bed Reactor Experiment

#### 3.1.1. Setup

The experiments were performed in a 1/2" stainless-steel tube reactor with an inner diameter of 9.7 mm placed inside an oven (see Figure 2). The oven (MUT Advanced Heating, Typ RRO 75/1000-1200 PN16, Jena, Germany) is 120 cm long and consists of three individually heated segments, providing both additional heating of the inlet gas mixture and a homogeneous temperature profile over the catalysts bed with a length of 25 cm, placed in the middle of the oven. Gas inlet was realized with a combination of mass flow controllers (MFCs, Brooks Instrument GmbH, Dresden, Germany and Bronkhorst Deutschland Nord GmbH, Kamen, Germany) and an evaporator system (aDROP Feuchtemeßtechnik GmbH, Fürth, Germany) producing steam at temperatures up to 870 K. The pipes transporting the gases and water vapor toward the oven were heated above 250 °C to prevent condensation of water. Detailed temperature measurements were conducted with two 2 m long thermocouples that could be moved inside a 3 mm and 6 mm housing through the catalyst bed and along the outer wall of the reactor, respectively. This enables measuring the temperature profile over the reactor length resulting from the endothermic reaction, with a resolution of up to 0.5 cm, once steady state is reached. Steady state refers here to a stable temperature in the reactor bed and a stable outlet concentration and flow rate, if sufficient time has passed, typically around 10 min, after the inlet conditions were changed and the system was moved out of equilibrium. The product gas was cooled down to room temperature to remove residual water for both system pressure control via a proportional relieve valve and gas analytics via infra-red sensors measuring the concentration of CH<sub>4</sub>, CO<sub>2</sub> and CO together with a thermal conductivity detector for hydrogen (Pronova Analysentechnik GmbH & Co. KG, Berlin, Germany). The flow rate after condensation is measured with a volumetric gas meter (Dr.-Ing. RITTER Apparatebau GmbH & Co. KG, Bochum, Germany) to calculate the amount of substance of the outlet species to further determine the conversion rates and selectivity of the process. Pressure sensors were installed at the inlet and outlet of the reactor to determine the system pressure and the pressure drop in the catalyst bed.

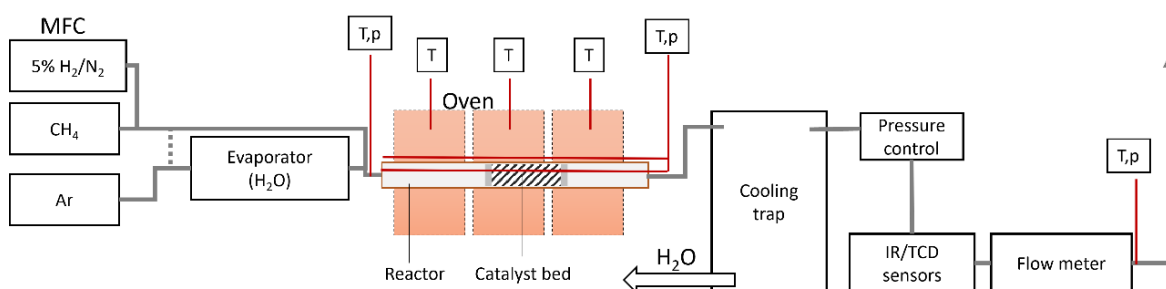


**Figure 2.** Experimental setup with MFCs to control the individual gas flow rates, evaporator, temperature (T) and pressure (p) measurements, cooling trap to remove residual water, pressure control for system pressure adjustment, gas analytics via infrared and thermal conductivity detector, and flow meter.

This setup allows for an accurate estimation of the reaction kinetics inside the catalyst bed and the associated temperature drop due to the endothermic reaction. Further characterization of the temperature-dependent kinetics is possible by variation in the gas hourly space velocity (GHSV), the system pressure, as well as the oven temperature and by analyzing the resulting temperature profile over the catalyst length and gas composition at the reactor outlet.

### 3.1.2. Catalyst and Characterization

The methane steam reforming catalyst consists of a Ni/NiO-based catalyst on 2 mm alumina spheres produced by Shell Catalyst and Technologies. According to the manufacturer, catalyst loading was 10–20 wt% NiO with a surface area of 6.17 m<sup>2</sup>/g (BET). SEM and EDX measurements (Mira3, Tescan, Brno-Kohoutovice, Czech Republic) were performed (see Figure 3) to characterize the surface structure and elemental composition of the fresh and used samples after steam reforming experiments at temperatures up to 1120 K, both for the outer surface of the spheres and in cross section, after breaking the spheres in the middle. In general, the nickel concentration is high at the surface, with up to 55 wt% Ni and a concentration gradient toward the center of the spheres up to 10 wt%. The morphology changes, after the steam reforming, toward bigger Ni particles due to surface agglomeration.

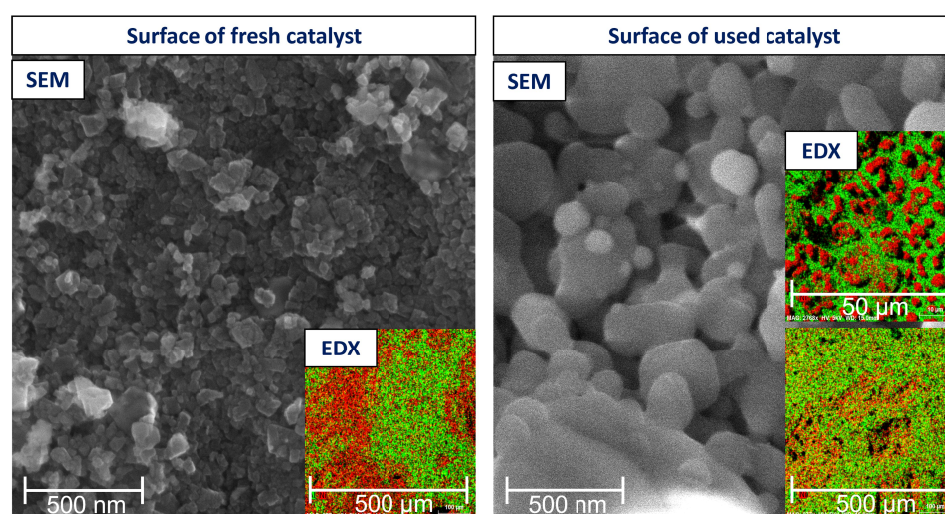


**Figure 3.** SEM and EDX pictures of the catalysts spheres (**left**) for the fresh sample and (**right**) for the used samples after steam reforming at temperatures up to 1120 K. Agglomeration of the particles (Ni in red, Al in green) could be observed.



However, after several experiments at varying conditions and after additional longtime measurements for more than 150 h, no significant drop in the conversion rate, as well as no changes in the temperature profile, could be observed, which may indicate a critical change in the active surface area of the catalyst. In fact, the temperature profile confirms that the reaction rates at temperatures of 970 K and above are that high and all the inlet species are converted to an equilibrium state, starting at the entrance to 5 cm inside of the catalyst bed. This state is defined by the expected conversion rate from thermodynamic equilibrium at the local catalyst bed temperature and pressure. This leads to a significant temperature drop that may be accompanied by carbon formation, specifically if temperatures drop below 870 K with a relatively low steam-to-carbon ratio of 2.

To prevent carbon formation and to obtain more precise information on the overall kinetics, the catalyst spheres were diluted with inert alumina spheres of 2.3 mm diameter, effectively reducing the size of the active surface area quite easily to the desired amount. This approach, however, may result in an uneven distribution of the active catalyst spheres and the possibility that not all the gas has contact with active surface, especially if the dilution is high. Consequently, locally uneven temperature profiles with additional minima over the catalyst bed length were observed and will be discussed in Section 6, *Results and Discussion*.

### 3.1.3. Experimental Procedure

For the measurements, the oven was heated up to a temperature of 1020 K under a small flow of inert Argon to remove any residual gas from the reactor and catalyst bed. Prior to performing the first experiments, the catalyst was activated by reducing nickel oxide to metallic nickel with a gas mixture of 5 % H<sub>2</sub> in nitrogen until the gas composition downstream of the catalyst was the same as the inlet gas. Afterwards, CH<sub>4</sub> and H<sub>2</sub>O were introduced at specific flow rates according to a GHSV of 1000 to 6000 1/h, a steam-to-carbon ratio of 2 and an absolute pressure of 1 bar. GHSV is calculated as the inlet flow rate at standard conditions divided by the volume of the catalyst bed. The temperature profile was measured when steady state was reached; that is to say, the temperature measured 5 cm into the catalyst bed, as well as the measured gas concentration and flow rate at the outlet, did not change anymore.

### 3.2. Monolith Experiment from Literature

Next to the experimental fixed-bed reactor setup, a steady-state monolithic reactor experiment from the literature [27] was used for mechanism verification. The reactor from [27] was made of ceramic material and stainless steel. Three cordierite honeycomb monoliths, each 1 cm in length with a diameter of 1.5 cm, were placed inside a ceramic reactor tube inside an oven. Each of the 89 monolith channels was rectangular with an inner hydraulic diameter of 1.13 mm. Two monoliths in front and at the end of the setup did not contain catalysts. The active monolith in the middle did not contain a washcoat underneath the catalyst to avoid any transport limitation within the catalyst layer. Within the experimental campaign, the varying mass flow of the reactants—water and methane—leads to steam/methane ratios (S/C) of one to four. In [27], a 2D approach was used for the simulations and the development of the mechanism presented [27]. This study only considers the experiments with an S/C ratio of 2.77 at four different temperatures with Argon (75 vol.%) as the carrier gas for the simulation. The hydraulic flow velocity in the single channels is set to 0.056 m/s. Isothermal conditions and a uniform inlet flow were established. More detailed information about the experiment can be found in [27].

## 4. 1D Simulations Setup

In the following section, the 1D model setup conditions are given for both experiments simulated within this work. The geometrical parameters for the two different setups are taken directly from the experiments. The experiments are simulated comparing the detailed reaction mechanism from [27] and the revised reaction mechanism from this work. The thermodynamic data are based on NASA polynomials from [38]. The heat flux from the

external oven is taken into account by radial heat exchange between the catalyst and its surrounding. Each simulation was carried out until steady state was reached, resulting in a simulation time of 120 s for the experimental setup with a 25 cm reactor and 5 s for the setup from the literature.

For the simulation of the 25 cm long experimental catalyst, a representative circular single-channel was used and split into 25 equidistant cells. The discretization into 25 cells was tested in a preliminary trial. The steady inlet gas species concentration and gas conditions can be seen in Table 1. The presented values for pressure, temperature and mass flow in the fixed-bed reactor correspond to the different GHSV from 1000 1/h to 6000 1/h. The physical reactor parameters for the model reactor are similar to the experimental reactor and can be found in Table 2.

**Table 1.** Steady inlet gas parameters for 1D model reactor simulation of two experiments.

Parameter	Unit	Fixed-Bed Reactor Experiment (with Increasing GHSV)	Monolith Experiment from [27]
Inlet gas composition	Mole fraction (-)	CH <sub>4</sub> : 0.33; H <sub>2</sub> O: 0.67	CH <sub>4</sub> : 0.07; H <sub>2</sub> O: 0.18; Ar: 0.75
Inlet gas temperature	K	1013.25	573.15
Initial catalyst surface temperature	K	998.95, 974.85, 954.2, 939.3, 934.0, 928.50	922.89, 1020.28, 1119.93, 1215.35
Ambient (oven) temperature	K	1012.00, 1005.10, 997.50, 992.50, 989.30, 987.50	922.89, 1020.28, 1119.93, 1215.35
Inlet gas pressure	10 <sup>5</sup> Pa	1.02, 1.02, 1.02, 1.03, 1.03, 1.03	1.01
Inlet mass flow	10 <sup>-6</sup> kg/s	3.30, 6.60, 9.90, 13.20, 16.5, 19.8	-
Inlet velocity	m/s	-	0.056

For the fixed-bed reactor experiment, 12 separate simulations were performed, one for each GHSV value ranging from 1000 to 6000 1/h. The 1D reactor model was used, and the reaction mechanism from [27] was compared to the mechanism with the adjusted Arrhenius parameters from this work. Each simulation was carried out for a simulation time of 120 s to make sure that the results reached steady state. The simulations were carried out on an AMD Opteron Processor 2389@2900 MHz system on eight CPUs simultaneously with a CPU time of 50 min and available RAM of 32 GB.

For the monolith experiment, four separate simulations were performed, one for each oven temperature value ranging from 923 to 1215 K. Again, the 1D reactor model and the reaction mechanism with the adjusted Arrhenius parameters from this work were used. The purpose of this experiment was to validate the newly introduced Arrhenius parameters, not only as an adaptation to the controlled conditions in our experiment but also to assess their performance under different conditions in other experiments. The 1D simulations of the monolith experiment from [27] with an S/C ratio of 2.77 were performed using a single-channel setup with 3 cm length split into 25 cells. Again, a preliminary trial was used to find the best discretization. The inlet gas composition and the gas parameters are listed in Table 1 and presented in [27]. All geometric parameters can be found in Table 2 and are in accordance with the experiment described in [27].

Furthermore, these simulations were carried out on an AMD Opteron Processor 2389@2900MHz system with an available RAM of 32 GB. Each single-channel simulation was calculated on eight CPUs simultaneously, which took 15 min.

**Table 2.** Physical input parameters for 1D model reactor simulation of two experiments.

Parameter	Unit	Fixed-Bed Reactor Experiment	Monolith Experiment from [27]
Catalyst outer geometry	-	Circular	Circular
Channel geometry	-	Quadratic	Quadratic
Number of cell	-	25	25
Channel density	$10^{+5}$ 1/m <sup>2</sup>	9.30	5.04
Axial heat conductivity	W/mK	$1.00 \times 10^{-1}$	85.0
Catalyst length	m	$2.5 \times 10^{-1}$	$3.00 \times 10^{-2}$
Catalyst radius	$10^{-3}$ m	4.85	7.5
Hydraulic diameter	m	$9.72 \times 10^{-4}$	$1.13 \times 10^{-3}$
Surface area per catalyst length	m <sup>2</sup> /m	$1.00 \times 10^{-1}$	$1.00 \times 10^{-2}$

## 5. Surface Chemistry Description and Development

The reaction mechanism on methane and water decomposition on nickel (Ni), as adjusted in the present paper, is based on [27] and was fitted using the GHSV 3000 1/h fixed-bed reactor experiment. The mechanism involves 13 surface species (e.g., Ni(s), CH<sub>4</sub>(s), or CO(s)) and 42 reactions with the Langmuir–Hinshelwood approach, which describes the interaction between a reactive surface and molecules in the gas phase that adsorb and react on the surface, followed by the desorption of newly formed molecules. Table 3 summarizes the Arrhenius parameters of the reactions and shows the changes that were made within this work for reaction numbers 2, 12 and 13, which are the desorption of H<sub>2</sub> (R2) and CO (R12) from the catalytic surface and the initial dissociation of CH<sub>4</sub> to CH<sub>3</sub> on the surface (R13). For these reactions, new Arrhenius parameters were introduced. The other reactions remained unchanged, as presented in [27]. The reaction rates altered in this work have been found to be highly sensitive within the mechanism by performing a sensitivity analysis, as described in [34]. Therein, the sensitivity analysis is explained as a method used to investigate the change in a quantity of interest due to small changes in controlling parameters. This is useful for gaining insight into the reaction model. Local sensitivity analysis involves calculating the partial derivative of the species source terms by changing the reaction rates of the kinetic model. So, the sensitivity analysis can be used to investigate the sensitivities of parameters such as species concentrations and gas temperature. In this study, the sensitivity analysis was performed by investigating how small changes in reaction rates have an influence on the gas temperature at a specific cell in the catalyst. In this work, the cell number 3 was used as the specific cell at position 0.025 m along the catalyst bed. It was chosen for the analysis due to the fact that, at this position, the reaction is in the endothermic phase and not in equilibrium.

In Figure 4, the result of the sensitivity analysis is shown. The analysis was performed for the setup in the fixed-bed reactor with GHSV 3000 1/h and the original reaction mechanism of [27]. The results show the most sensitive reactions in descending order of influence on the simulation results. The negative bars symbolize a reduction in the total reaction rate, and the results in the positive range symbolize an increase in the total rate when the individual reaction rate is increased. Following the sensitivity analysis, the rate parameters, such as pre-factor, temperature exponent, and activation energy of each of the listed reactions, were revised and adjusted manually, in accordance with the experimental data. It can be seen from these results that CO adsorption (R11) has a strong influence on the simulation results. However, in the case of (R11), a reduction in the sticking rate was found to cause a deterioration in the overall result. Increasing the sticking coefficient, as can be seen from the analysis, did not cause any more significant changes in the results. On the contrary, an increase in the CO desorption rate (R12) yielded a significant improvement for the overall simulation result. This may be because CO was obstructing active or adsorption sites, thereby blocking the reaction pathways for other crucial reactions. When the surface is highly covered by CO, the reaction rate of other reactions is effectively reduced, as neighboring sites are not available for interaction. The same result was also observed for the adsorption (R1) and desorption of H<sub>2</sub> (R2). Increasing the desorption rate produced

the required results. The exact amount of adjustment was determined step by step, in alignment with the experiments, just as which of the three parameters had the desired effect on the overall quality of the results. The axially resolved temperature profile of the experiments was utilized to aid in adjusting the kinetics, rather than solely relying on reactor outlet concentrations, which indicates the close equilibrium state. This allowed for the fine-tuning of the reaction rates for the best results.

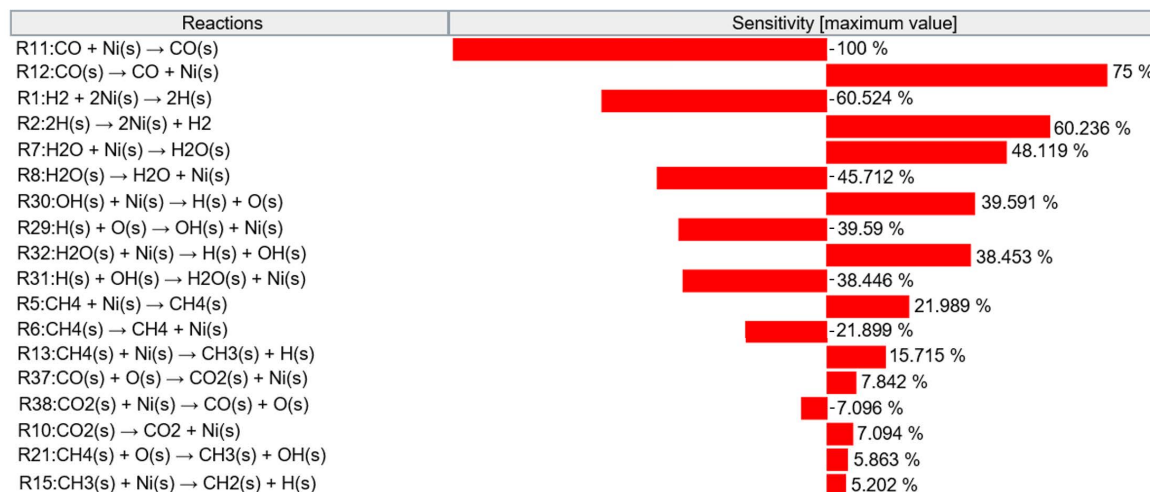


**Figure 4.** Reaction sensitivity analysis in percentage for fixed-bed reactor simulation setup at GHSV 3000 1/h with reaction mechanism of [27].

In this way, the sensitive reactions were systematically tested, and the changes made for the three reactions, as presented in Table 3, were found to particularly improve the simulation results. For (R2), the pre-exponential factor was increased by a factor of 100. Further, for (R12), the pre-exponential factor, the temperature coefficient and the activation energy were adjusted, as originally given in [27], with  $3.563 \times 10^{11}$ , 0.0 and 111.27, respectively. Finally, the pre-exponential factor of (R13) was increased from  $3.700 \times 10^{21}$  and the activation energy decreased from 57.70 kJ/mol. Adjustments to further reaction rates did not result in any improvement in the simulation results.

**Table 3.** Surface reaction mechanism based on [27] with revision from this work (s.c.—sticking coefficient).

Reaction	$A_r$ (cm, mol, s)	$\beta_r$ (-)	$E_r$ (kJ/mol)	Revision	
R1	$H_2 + 2Ni(s) \rightarrow 2H(s)$	$1.000 \times 10^{-2}$	0.00	s.c.	
R2	$2H(s) \rightarrow 2Ni(s) + H_2$	$2.545 \times 10^{+21}$	0.00	81.21	This work
R3	$O_2 + 2Ni(s) \rightarrow 2O(s)$	$1.000 \times 10^{-2}$	0.00	s.c.	
R4	$2O(s) \rightarrow 2Ni(s) + O_2$	$4.283 \times 10^{+23}$	0.00	474.95	
R5	$CH_4 + Ni(s) \rightarrow CH_4(s)$	$8.000 \times 10^{-3}$	0.00	s.c.	
R6	$CH_4(s) \rightarrow CH_4 + Ni(s)$	$8.705 \times 10^{+15}$	0.00	37.55	
R7	$H_2O + Ni(s) \rightarrow H_2O(s)$	$1.000 \times 10^{-1}$	0.00	s.c.	
R8	$H_2O(s) \rightarrow H_2O + Ni(s)$	$3.732 \times 10^{+12}$	0.00	60.79	
R9	$CO_2 + Ni(s) \rightarrow CO_2(s)$	$1.000 \times 10^{-5}$	0.00	s.c.	
R10	$CO_2(s) \rightarrow CO_2 + Ni(s)$	$6.447 \times 10^{+7}$	0.00	25.98	
R11	$CO + Ni(s) \rightarrow CO(s)$	$5.000 \times 10^{-1}$	0.00	s.c.	
R12	$CO(s) \rightarrow CO + Ni(s)$	$5.660 \times 10^{+11}$	0.70	111.00	This work
	Coverage /CO(s)	0.00	0.00	-50.00	
R13	$CH_4(s) + Ni(s) \rightarrow CH_3(s) + H(s)$	$4.440 \times 10^{+21}$	0.00	40.40	This work
R14	$CH_3(s) + H(s) \rightarrow CH_4(s) + Ni(s)$	$6.034 \times 10^{+21}$	0.00	61.58	

Table 3. Cont.

	Reaction	$A_r$ (cm, mol, s)	$\beta_r$ (-)	$E_r$ (kJ/mol)	Revision
R15	$\text{CH}_3(\text{s}) + \text{Ni}(\text{s}) \rightarrow \text{CH}_2(\text{s}) + \text{H}(\text{s})$	$3.700 \times 10^{+24}$	0.00	100.00	
R16	$\text{CH}_2(\text{s}) + \text{H}(\text{s}) \rightarrow \text{CH}_3(\text{s}) + \text{Ni}(\text{s})$	$1.293 \times 10^{+23}$	0.00	55.33	
R17	$\text{CH}_2(\text{s}) + \text{Ni}(\text{s}) \rightarrow \text{CH}(\text{s}) + \text{H}(\text{s})$	$3.700 \times 10^{+24}$	0.00	97.10	
R18	$\text{CH}(\text{s}) + \text{H}(\text{s}) \rightarrow \text{CH}_2(\text{s}) + \text{Ni}(\text{s})$	$4.089 \times 10^{+24}$	0.00	79.18	
R19	$\text{CH}(\text{s}) + \text{Ni}(\text{s}) \rightarrow \text{C}(\text{s}) + \text{H}(\text{s})$	$3.700 \times 10^{+21}$	0.00	18.80	
R20	$\text{C}(\text{s}) + \text{H}(\text{s}) \rightarrow \text{CH}(\text{s}) + \text{Ni}(\text{s})$	$4.562 \times 10^{+22}$	0.00	161.11	
R21	$\text{CH}_4(\text{s}) + \text{O}(\text{s}) \rightarrow \text{CH}_3(\text{s}) + \text{OH}(\text{s})$	$1.700 \times 10^{+24}$	0.00	88.30	
R22	$\text{CH}_3(\text{s}) + \text{OH}(\text{s}) \rightarrow \text{CH}_4(\text{s}) + \text{O}(\text{s})$	$9.876 \times 10^{+22}$	0.00	30.37	
R23	$\text{CH}_3(\text{s}) + \text{O}(\text{s}) \rightarrow \text{CH}_2(\text{s}) + \text{OH}(\text{s})$	$3.700 \times 10^{+24}$	0.00	130.10	
R24	$\text{CH}_2(\text{s}) + \text{OH}(\text{s}) \rightarrow \text{CH}_3(\text{s}) + \text{O}(\text{s})$	$4.607 \times 10^{+21}$	0.00	23.62	
R25	$\text{CH}_2(\text{s}) + \text{O}(\text{s}) \rightarrow \text{CH}(\text{s}) + \text{OH}(\text{s})$	$3.700 \times 10^{+24}$	0.00	126.80	
R26	$\text{CH}(\text{s}) + \text{OH}(\text{s}) \rightarrow \text{CH}_2(\text{s}) + \text{O}(\text{s})$	$1.457 \times 10^{+23}$	0.00	47.07	
R27	$\text{CH}(\text{s}) + \text{O}(\text{s}) \rightarrow \text{C}(\text{s}) + \text{OH}(\text{s})$	$3.700 \times 10^{+21}$	0.00	48.10	
R28	$\text{C}(\text{s}) + \text{OH}(\text{s}) \rightarrow \text{CH}(\text{s}) + \text{O}(\text{s})$	$1.625 \times 10^{+21}$	0.00	128.61	
R29	$\text{H}(\text{s}) + \text{O}(\text{s}) \rightarrow \text{OH}(\text{s}) + \text{Ni}(\text{s})$	$5.000 \times 10^{+22}$	0.00	97.90	
R30	$\text{OH}(\text{s}) + \text{Ni}(\text{s}) \rightarrow \text{H}(\text{s}) + \text{O}(\text{s})$	$1.781 \times 10^{+21}$	0.00	36.09	
R31	$\text{H}(\text{s}) + \text{OH}(\text{s}) \rightarrow \text{H}_2\text{O}(\text{s}) + \text{Ni}(\text{s})$	$3.000 \times 10^{+20}$	0.00	42.70	
R32	$\text{H}_2\text{O}(\text{s}) + \text{Ni}(\text{s}) \rightarrow \text{H}(\text{s}) + \text{OH}(\text{s})$	$2.271 \times 10^{+21}$	0.00	91.76	
R33	$\text{OH}(\text{s}) + \text{OH}(\text{s}) \rightarrow \text{H}_2\text{O}(\text{s}) + \text{O}(\text{s})$	$3.000 \times 10^{+21}$	0.00	100.00	
R34	$\text{H}_2\text{O}(\text{s}) + \text{O}(\text{s}) \rightarrow \text{OH}(\text{s}) + \text{OH}(\text{s})$	$6.373 \times 10^{+23}$	0.00	210.86	
R35	$\text{C}(\text{s}) + \text{O}(\text{s}) \rightarrow \text{CO}(\text{s}) + \text{Ni}(\text{s})$	$5.200 \times 10^{+23}$	0.00	148.10	
R36	$\text{CO}(\text{s}) + \text{Ni}(\text{s}) \rightarrow \text{C}(\text{s}) + \text{O}(\text{s})$	$1.354 \times 10^{+22}$	-3.00	116.12	
	Coverage /CO(s)	0.00	0.00	-50.00	
R37	$\text{CO}(\text{s}) + \text{O}(\text{s}) \rightarrow \text{CO}_2(\text{s}) + \text{Ni}(\text{s})$	$2.000 \times 10^{+19}$	0.00	123.60	
	Coverage /CO(s)	0.00	0.00	-50.00	
R38	$\text{CO}_2(\text{s}) + \text{Ni}(\text{s}) \rightarrow \text{CO}(\text{s}) + \text{O}(\text{s})$	$4.653 \times 10^{+23}$	-1.00	89.32	
R39	$\text{CO}(\text{s}) + \text{H}(\text{s}) \rightarrow \text{HCO}(\text{s}) + \text{Ni}(\text{s})$	$4.019 \times 10^{+20}$	-1.00	132.23	
R40	$\text{HCO}(\text{s}) + \text{Ni}(\text{s}) \rightarrow \text{CO}(\text{s}) + \text{H}(\text{s})$	$3.700 \times 10^{+21}$	0.00	0.00	
	Coverage /CO(s)	0.00	0.00	-50.00	
R41	$\text{HCO}(\text{s}) + \text{Ni}(\text{s}) \rightarrow \text{CH}(\text{s}) + \text{O}(\text{s})$	$3.700 \times 10^{+24}$	-3.00	95.80	
R42	$\text{CH}(\text{s}) + \text{O}(\text{s}) \rightarrow \text{HCO}(\text{s}) + \text{Ni}(\text{s})$	$4.604 \times 10^{+20}$	0.00	109.97	

## 6. Results and Discussion

In the following section, the simulation results for both presented experiments are discussed.

### 6.1. Fixed-Bed Reactor Experiments

Figure 5 shows the temperature profile along the catalytic reactor as a function of catalyst length. The temperature profile was measured for six different GHSVs and is here compared to the 1D simulation result using two different reaction mechanisms: the kinetic reaction mechanism presented in [27] in comparison with the revised mechanism in this work. Both simulations depicted as a dashed line and a solid line were calculated using the described 1D tool from Section 2, *Model Description*, with the same physical settings. The only difference here was the given Arrhenius parameters for the revised three reactions.

By looking at the curves for each GHSV, it is clear that the adjusted reaction mechanism consistently shows better agreement with the experiments than the reaction mechanism presented in the literature by [27]. This is primarily due to the fact that only experiments examining the results of steam reforming at the outlet were available for developing the mechanism in [27]. This can result in the mechanism being adjusted to nearly equilibrium and the kinetics not being fully captured. However, with the support of the axially resolved temperature profile, it was possible to more accurately address this.

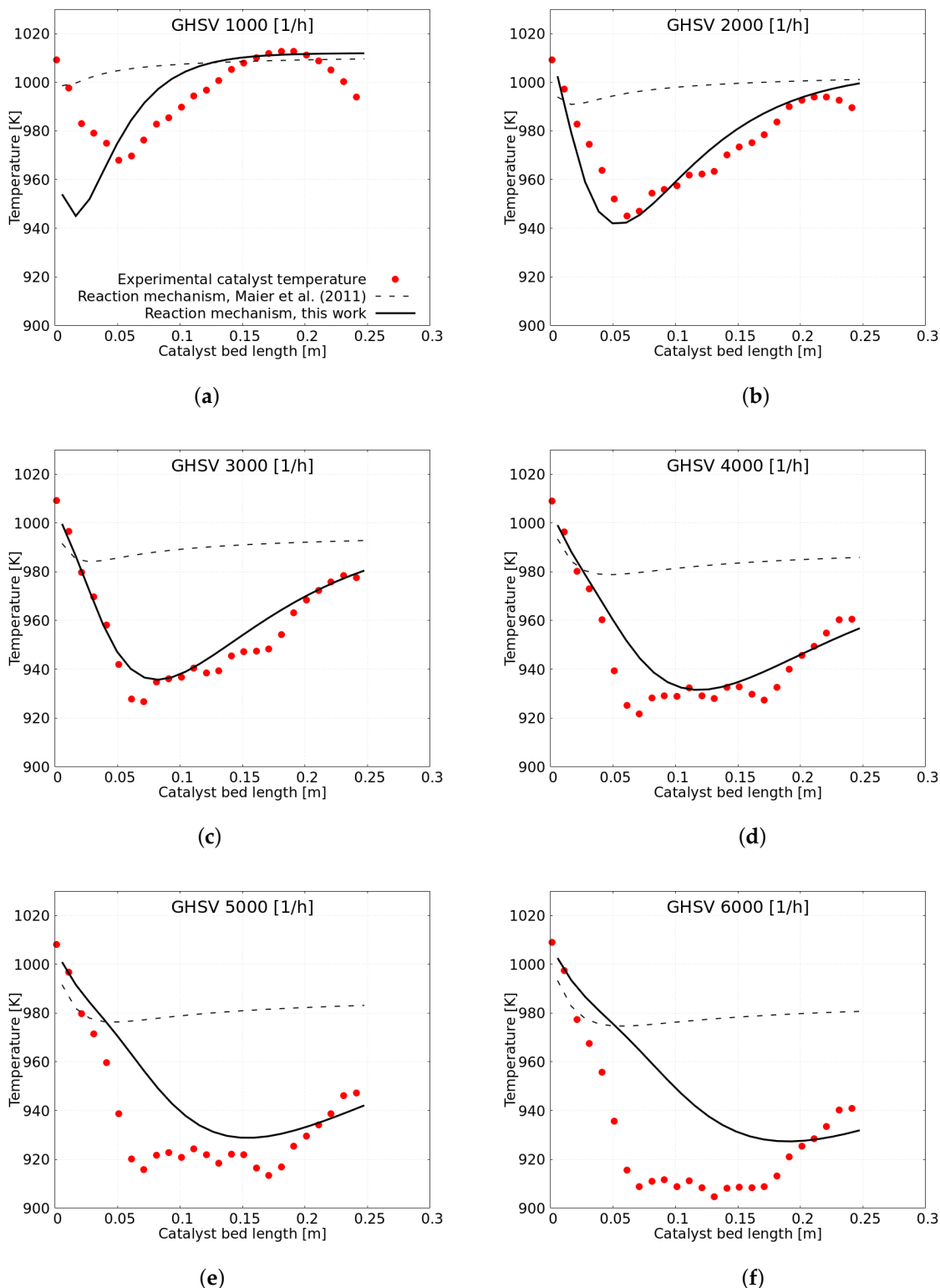


**Figure 5.** Measured and 1D simulated temperature profiles over the catalyst length for (a) GHSV 1000 1/h, (b) GHSV 2000 1/h, (c) GHSV 3000 1/h, (d) GHSV 4000, (e) GHSV 5000 and (f) GHSV 6000 1/h for the experiments in the fixed-bed reactor. Closed circles represent experimental results, dashed lines represent 1D simulation results with reaction mechanism of [27] and solid lines represent 1D simulation results with reaction mechanism revised in this work.

Particularly noteworthy is that the fitted reaction mechanism matches the shift along the reactor axis of the temperature minimum with increasing GHSV. With the exception of GHSV 1000 1/h and GHSV 6000 1/h, it can be seen that the mechanism presented here is able to predict the experimental range of minimum temperatures. This deviation between the results of 1D simulation and the experiment for GHSV of 1000 1/h and 6000 1/h are due to differences in the distribution of the catalyst. In the 1D simulation reactor, an evenly distributed active surface area was used, whereas in the experiments, because of the dilution with inert Ni/Al<sub>2</sub>O<sub>3</sub> spheres, the active surface area was comparatively high only locally in areas with catalyst spheres that have a high surface area. However, active area may average over the whole catalyst bed to the same values used in simulation. For GHSV 1000 1/h, the mass flow is relatively low, as is the residence time in the reactor high, so that, in simulation, the active surface area is enough to convert most of the gas close to the inlet (compare Figure 6a, where a stable concentration is calculated at 0.1 m). However, in the experiment, the gas would only react with the randomly distributed spheres, which would already extend the reaction zone, as not all of the gas reacts on the first sphere, leading to a smaller temperature drop compared to the simulation. Increasing the mass flow with higher GHSV leads to the extension of the reaction zone both in the simulation and in the experiments, as the surface area is limited in both cases. However, due to the higher amount of gas, more gas would react over the single catalyst spheres, leading to an increased temperature drop in the experiments. For a GHSV up to 5000 1/h, simulation and experiments converge to a similar temperature profile. For higher flow rates, the local temperature drop near the catalyst spheres is measured more pronounced, as more gases react locally, also leading to an uneven temperature profile. At GHSV 5000 1/h and above, this leads to a higher initial temperature drop. As mentioned, unlike the experiments, for all simulations, a uniform catalytic active surface along the entire reactor is assumed. This leads to continuous curves in the simulation results compared to the experiment. In the simulation, the outlet concentration would not match the equilibrium values for higher GHSV, as reactions would be slowed down due to the limited active surface area. Comparatively, in the experiments, this may also be the case but is further complicated, as part of the inlet gases reacts at different points, but reasonably quickly, and at different temperatures over the catalyst bed. This makes it difficult to match and compare the measured outlet composition and gas outlet temperature with the expected equilibrium composition.

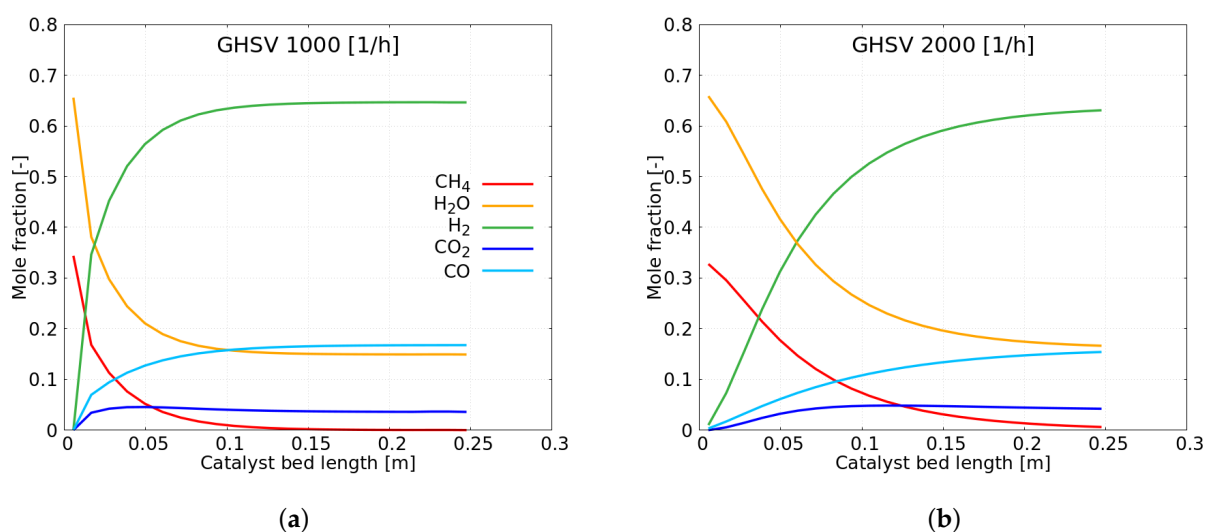
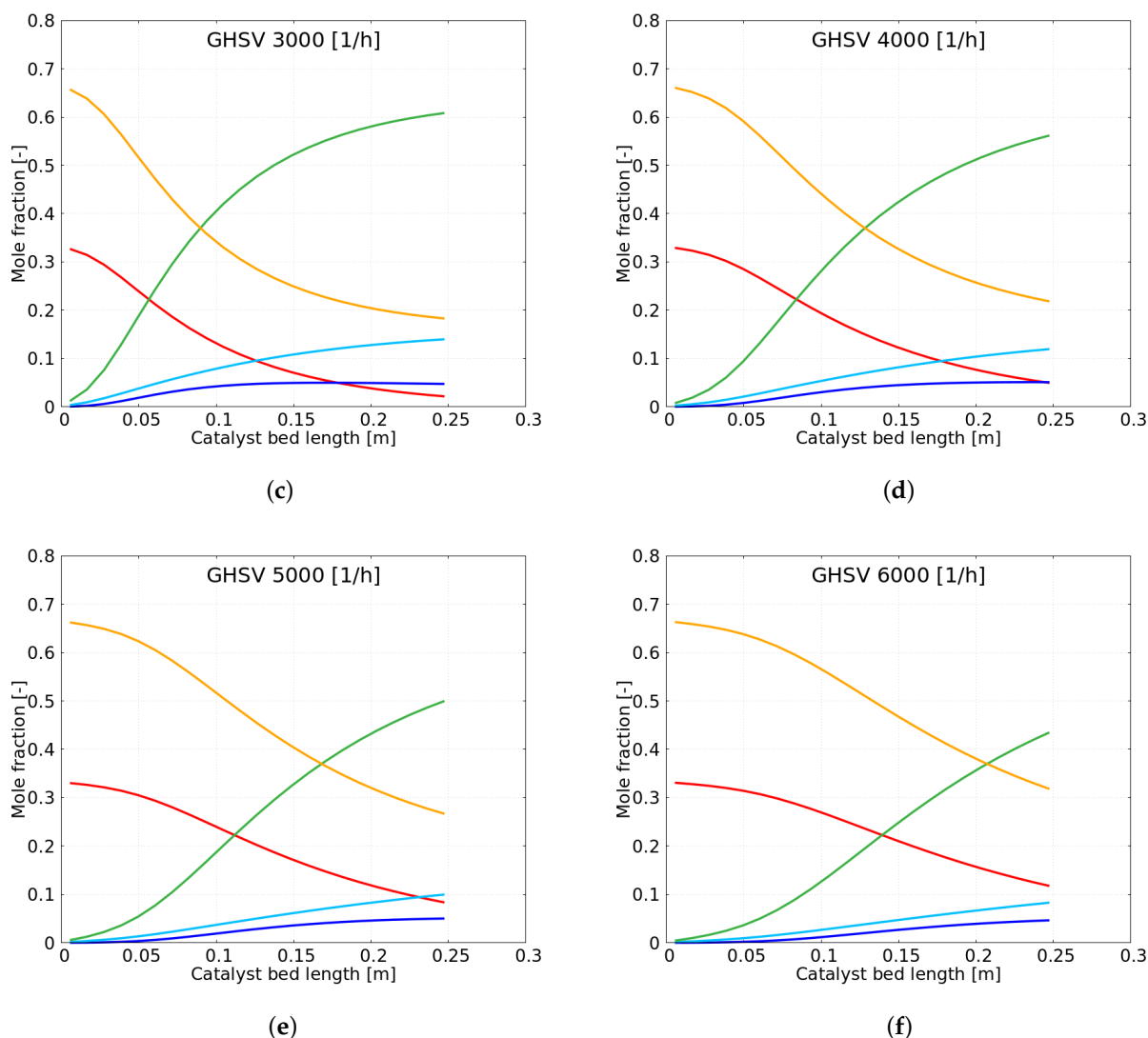


Figure 6. Cont.



**Figure 6.** 1D simulated gas composition profile for lines red CH<sub>4</sub>, orange H<sub>2</sub>O, green H<sub>2</sub>, dark blue CO<sub>2</sub> and light blue CO over the catalyst length for (a) GHSV 1000 1/h, (b) GHSV 2000 1/h, (c) GHSV 3000, (d) GHSV 4000 1/h, (e) GHSV 5000 and (f) GHSV 6000 1/h with revised reaction mechanism from this work.

The temperature drop in GHSV 1000 1/h at 0.2 m (see Figure 5a) in the experiment is due to the temperature profile of the oven, which is even in the middle but decreases to its end in this area. This was not reflected in the simulation, as a uniform oven with a constant outer temperature was assumed though it was slightly corrected for each GHSV (see Table 1). This drop is mitigated at higher flow rates because of convective heat transport along the direction of the gas flow and the drop of the gas outlet temperature below the oven temperature. The differences in simulations for GHSV 5000 1/h and 6000 1/h are further pronounced due to deviation in the catalyst distribution over the length of the catalyst.

In Figure 7, the experimental and modeled catalyst outlet gas compositions are compared. Again, the 1D simulation results for the two different mechanisms are shown. A separate simulation was performed for each GHSV until a steady state of the simulation results was reached. The outlet concentrations are represented as a function of the GHSV. It becomes visible that the prediction accuracy of the reaction mechanism introduced in this work is substantially higher than the unfitted mechanism. For a GHSV of 1000 1/h, a slight discrepancy between experiment and model can be observed. This discrepancy



goes together with the temperature deviation, as discussed above concerning Figure 5. It is worth noting that, at this GHSV, the simulation achieves the experimental temperature equilibrium more accurately than the experiment. This could be due to the uneven oven temperature at the end of the reactor and the resulting temperature drop after a reactor length of 0.2 m in the experiment, which prevented a complete attainment of equilibrium in the experiment. At GHSVs of 2000 1/h to 4000 1/h, the outlet concentrations as well as the temperature curves are mapped with high accuracy. The discrepancy for GHSV 5000 1/h and GHSV 6000 1/h can also be explained by the fact that the model in the area with high flow velocity was not quite able to map the temperature curve and kinetics and, thus, the outlet concentrations for this area. Provided that the active surface area of the catalyst is not limited, in the case of low GHSV, the outlet concentrations are primarily dependent on the gas outlet temperature both in experiment and in simulation and follow thermodynamic equilibrium for the involved gas species. Some discrepancy is again caused by the uneven distribution of the catalyst limiting the contact of the gas with the catalyst surface if the local catalyst concentration is low.

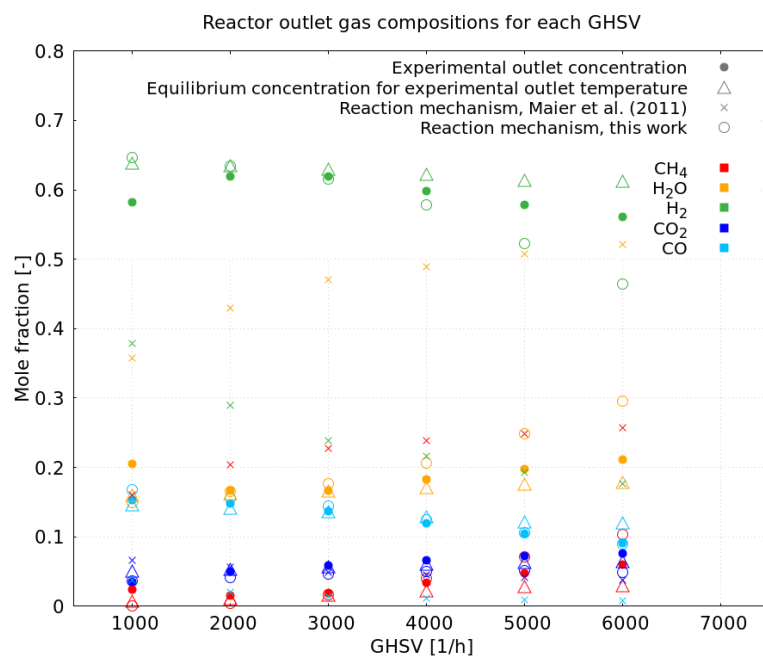


**Figure 7.** Reactor outlet gas composition over the varied GHSV with closed circles representing experimental results, open triangles representing the equilibrium concentration for the experimental outlet temperature, dashed lines representing 1D simulation results with reaction mechanism of [27] and solid lines with open circles representing 1D simulation results with reaction mechanism revised in this work.

The 1D model with the adjusted reaction mechanism provides the possibility to depict the gas concentration over the catalyst length, as shown in Figure 6. For GHSV 1000 1/h, it results in steady state after a catalyst length of 0.13 m, leading to a complete conversion of the CH<sub>4</sub> at the present temperature. For a strictly kinetic model where the kinetic or gas surface interaction is limited by the strongly reduced catalytic active surface area, higher GHSV depicts an incomplete conversion of CH<sub>4</sub>, depending on the mass flow. From a more practical point of view, temperature over the catalyst length is influenced by the amount of gas that is still able to react, the available catalytic surface area and the heat transfer from the oven. This would deviate from an equilibrium-based model where the gas concentration is determined by the temperature and pressure over the catalyst, provided that the reaction rate, surface size and gas phase–surface interaction (e.g., diffusion) are fast enough. The incomplete conversion for higher GHSV can be remedied with a stronger concentration of catalyst or an extension of the reactor length.

To illustrate this and to point out further application areas of the model, the simulation results from the kinetic approach in Figure 6 were compared with the expected gas-phase concentration at thermodynamic equilibrium depending on the calculated reactor temperature from Figure 5 for a GHSV of 1000 1/h and an assumed longer catalytic bed for 5000 1/h. Figure 8 shows that the kinetic mechanism approaches equilibrium concentration already at around 0.13 m at GHSV 1000 1/h when enough catalytic area is available but requires a longer catalyst bed for higher flow rates, reaching equilibrium levels at 0.45 m for 5000 1/h. The equilibrium compositions of the gases in Figure 8 were calculated using NASA polynomials.

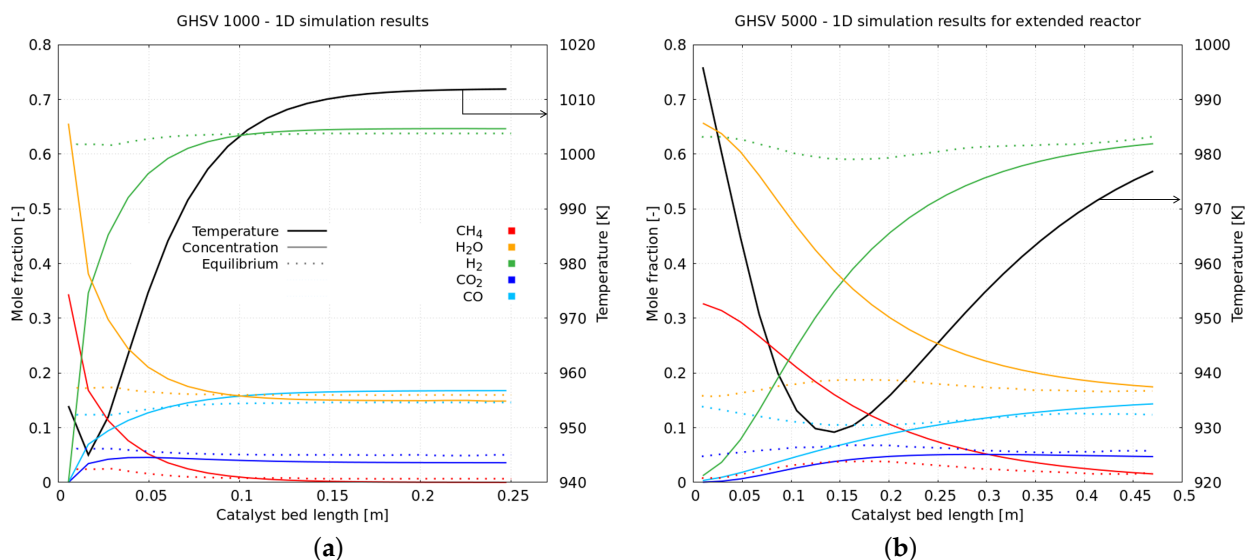


**Figure 8.** 1D simulated gas composition profile over the catalyst bed length for the (a) GHSV 1000 1/h and (b) GHSV 5000 1/h for extended reactor length with revised reaction mechanism from this work. Colored lines represent the gas composition at the specific catalyst bed length, dashed lines represent the equilibrium concentrations and the thicker black line represents corresponding temperature in the reactor.

### 6.2. Monolith Experiments from the Literature

In the previous chapter, the fitted mechanism demonstrates its performance. To further verify the revised kinetic model, the experiment from [27] is calculated using the 1D model reactor setup explained prior with the reaction mechanism adjusted in this work. The simulation was performed at four experimental temperatures for an S/C ratio of 2.77. As a result, it can be seen in Figure 9 that the revised mechanism is able to reproduce the experimental results of [27]. It is to be emphasized that the methane conversion is slightly over-predicted while the conversion of water is more close to the experiment than with the original mechanism. What is even more is that the trend of decreasing water conversion at temperatures higher than 1030 K can be slightly reflected by the model and reflects the equilibrium, whereas in the original simulation results of [27], an increase in the water conversion is shown. With this additional verification, it can be proven that the revised reaction mechanism is not purely adapted to our experiment but is also able to reproduce further experiments with reasonable accuracy.

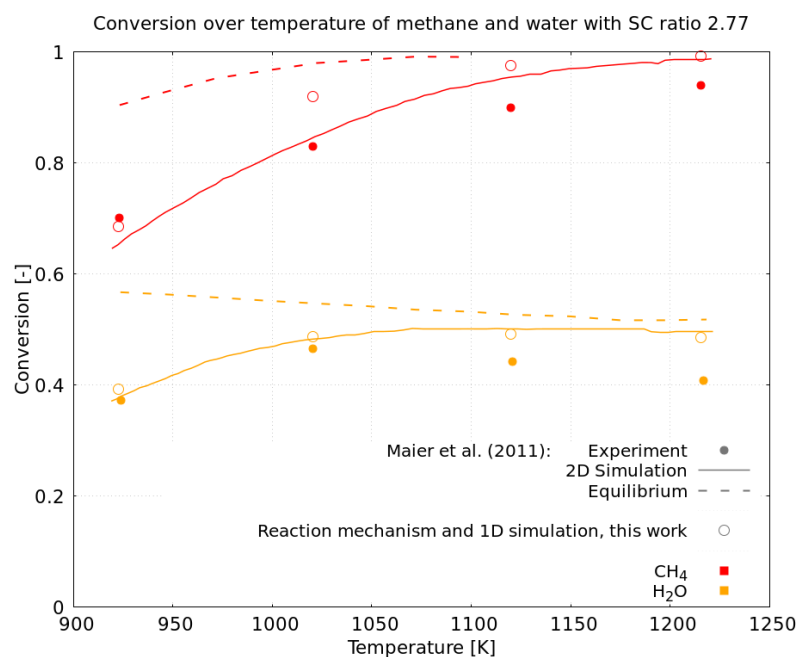


**Figure 9.** Methane and water conversion for  $S/C = 2.77$  and 75 % Argon with 1D simulation results using revised reaction mechanism developed within this work, compared to 2D simulation results and experiments presented in [27]. Closed circles represent experimental results from [27], dashed lines represent equilibrium from [27], solid lines represent 2D simulation results from [27] with reaction mechanism of [27] and open circles represent 1D simulation results with reaction mechanism revised in this work.

## 7. Conclusions

Within the scope of this work, a published MSR kinetic reaction mechanism was revised and new Arrhenius parameters for kinetic modeling were introduced using stationary fixed-bed reactor experiments for fitting the reaction mechanism. The new reaction mechanism was validated for a set of different conditions, with experiments performed in this work and also in the literature (see Table 4). The ability to measure the temperature profile along the length of the reactor was particularly helpful and provides insight into the reaction kinetics taking place; while measurements taken at the outlet of the catalyst often show nearly equilibrium conditions, the temperature profile shows that using data from close to equilibrium alone would not be sufficient to fully understand the reaction mechanism, especially in case of kinetic limitations either in the reaction rate or available surface area. The new experimental data allow for the more accurate modeling of the reaction. Additionally, by carefully controlling the surface dilution in the experiments, it was possible to slow down the catalyst conversion rate, which also aided in the improved determination of the reaction kinetics.

Subsequently, an experiment from the literature was used to further verify the adjusted mechanism. The newly introduced Arrhenius parameters in this work are able to reproduce both the experiments conducted in this study and the experiments presented in the literature. Three reaction rates were changed within this study. Two of the changed rates were from desorption reactions of  $H_2$  and  $CO$ , (R2) and (R12), respectively. These reactions were rate-determining due to the fact that before the increase in their rate, not enough  $H_2$  or  $CO$  could be detached from the surface to give surface reactions the space to happen. By accelerating the two desorption rates, space on the Ni surface was freed to provide room for the following reactions. The adjustment of the surface H abstraction reaction of adsorbed methane (R13) was also found to be beneficial for the overall performance of the mechanism due to the acceleration of the freed-up Ni surface.

**Table 4.** Conditions tested for new introduced reaction mechanism for two experiments with 1D model monolith reactor simulations.

Parameter	Unit	Fixed-Bed Reactor Experiment (with Increasing GHSV)	Monolith Experiment from [27]
S/C ratio	(-)	2.00	2.70
Temperature	K	1012.00, 1005.10, 997.50, 992.50, 989.30, 987.50	922.89, 1020.28, 1119.93, 1215.35
Pressure	$10^{+5}$ Pa	1.02, 1.02, 1.02, 1.03, 1.03, 1.03	1.01
GHSV	1/h	1000, 2000, 3000, 4000, 5000, 6000	9000

The 1D monolith reactor model used in this work was able to reproduce the experimental results within a short computational time using both reaction mechanisms. The reforming reactions adjusted for the mechanism proved to be fast enough and tended to reach equilibrium as they moved along the reformer length. It was shown that the model with the revised reaction mechanism has a wide range of applications, including the simulation of an extended reactor bed and the calculation of conversion rates along the catalyst, as shown in this work.

The simulation results for GHSV 1000 1/h, 5000 1/h and 6000 1/h show possible potential for further improving the kinetic mechanism. One other reason for the deviation might be the transfer of the physical properties of a fixed-bed to a monolithic model. Nevertheless, based on the overall results presented in this work, it can be observed that the use of the monolithic 1D catalyst model reactor yields satisfactory results for fixed-bed reactor experiments. However, in certain scenarios, a fixed-bed reactor model may help to better depict kinetic and mass transport phenomena and improve estimation on the residence times of the species and the gas flow in the reactor. Moreover, the kinetic model could be transferred from an irreversible, explicit approach, where Arrhenius parameters are specified for forward as well as backward reactions, as presented here, to an explicit equilibrium model. But this necessitates the use of reliable thermodynamic data on surface intermediate species, which are not easily available in the literature. Overall, the presented 1D tool and the introduced reaction mechanism are a fast and accurate way to obtain computationally cheap results for design and optimization of MSR over a nickel catalyst.

**Author Contributions:** Conceptualization, J.R., F.R., J.I. and F.M.; methodology, J.R., F.R., J.I., N.R., E.C. and F.M.; software, J.R., V.G. and F.M.; validation, J.R. and F.R.; formal analysis, J.R.; investigation, F.R., J.I., N.R. and E.C.; resources, F.M. and J.I.F.; data curation, J.R., F.R. and V.G.; writing—original draft preparation, J.R. and F.R.; writing—review and editing, J.R., F.R. and V.G.; visualization, J.R.; supervision, V.G., F.M. and J.I.F.; project administration, F.M. and J.I.F.; funding acquisition, F.M. and J.I.F. All authors have read and agreed to the published version of the manuscript.

**Funding:** This work was supported by the Federal Ministry for Economic Affairs and Climate Action (BMWK) (grant: FKZ 03EWS002A) and by the German Federal Government, the Federal Ministry of Education and Research and the State of Brandenburg within the framework of the joint project EIZ: Energy Innovation Center (project numbers: 85056897 and 03SF0693A) with funds from the Structural Development Act (Strukturstärkungsgesetz) for coal-mining regions.

**Institutional Review Board Statement:** Not applicable.

**Data Availability Statement:** No new data were created.

**Acknowledgments:** We thank the Federal Ministry for Economic Affairs and Climate Action (BMWK) (grant: FKZ 03EWS002A) and the German Federal Government, the Federal Ministry of Education and Research and the State of Brandenburg within the framework of the joint project EIZ: Energy Innovation Center (project numbers: 85056897 and 03SF0693A) with funds from the Structural Development Act (Strukturstärkungsgesetz) for coal-mining regions.

**Conflicts of Interest:** The authors declare no conflict of interest.

## Nomenclature

### Roman letters

$A$	Cross-sectional channel area ( $m^2$ )
$A_m$	Catalytic surface area in current cell ( $m^2$ )
$A_{w,G}$	Geometric surface area of the wall in the cell ( $m^2$ )
$c_p$	Specific heat capacity at constant pressure ( $J/(kg \cdot K)$ )
$C_{i,g}$	Concentration of species $i$ in the bulk gas ( $mol/m^3$ )
$C_{i,p}$	Concentration of species $i$ in the thin-film layer ( $mol/m^3$ )
$d_h$	Hydraulic diameter of the channel (m)
$dist_h$	Horizontal distance between representative channels (m)
$D_i$	Diffusion coefficient of species $i$ ( $m^2/s$ )
$D_T$	Thermal diffusion coefficient ( $m^2/s$ )
$f_F$	Friction factor (:)
$h_g$	Mean specific enthalpy of bulk gas ( $J/kg$ )
$h_{j,g \leftrightarrow p}$	Specific enthalpy of species $j$ transported between bulk gas and thin-film layer. If the species is transported from the bulk gas, the bulk gas enthalpy is used; if it is transported to the bulk gas, the thin-film layer enthalpy is used ( $J/kg$ )
$h_{j,m}$	Specific enthalpy of species $j$ in surface phase $m$ ( $J/kg$ )
$h_T$	Heat transfer coefficient ( $W/(m^2 \cdot K)$ )
$k_g$	Thermal conductivity ( $W/(m \cdot K)$ )
$k_{m,i}$	Mass transfer coefficient of species $i$ ( $m/s$ )
$k_s$	Thermal conductivity ( $W/(m \cdot K)$ )
$K_e$	Overall effectiveness factor (:)
$K_h$	Overall heat transfer factor (:)
$K_m$	Overall mass transfer factor (:)
$K_x$	Horizontal heat conductivity ( $W/(m \cdot K)$ )
$K_y$	Vertical heat conductivity ( $W/(m \cdot K)$ )
$m_g$	Gas mass in cell (kg)
$N_g$	Number of gas phase species
$N_{surf}$	Number of surface phases
$N_{s,m}$	Number of species in surface phase $m$
$Nu$	Nusselt number (:)
$Nu_{T,\infty}$	Asymptotic Nusselt number for constant flux boundary condition (:)
$p$	Pressure (Pa)
$P$	Geometric wetted perimeter of the channel (m)
$Pr$	Prandtl number (:)
$Re$	Reynolds number (:)
$Sc_i$	Schmidt number of species $i$ (:)
$Sh_i$	Sherwood number for species $i$ (:)
$Sh_{T,\infty}$	Asymptotic Sherwood number for constant flux boundary condition (:)
$t$	Time (s)
$T_a$	Ambient temperature (K)
$T_g$	Gas temperature (K)
$T_w$	Temperature of the wall and thin-film layer (K)
$v$	Fluid velocity along the channel (m/s)
$V_p$	Volume of the thin-film layer gas in the current cell ( $m^3$ )
$V_s$	Volume of the solid wall material (substrate) in the current cell ( $m^3$ )
$w$	Radial distance through the washcoat (m)
$W_i$	Molecular weight of species $i$ ( $kg/mol$ )
$Y_i$	Mass fraction of species $i$ (:)

**Greek letters**

$\Gamma_n$	site density of surface phase $n$ (mol/m <sup>2</sup> )
$\Delta x$	length of cell (m)
$\theta_i$	site fraction of species $i$ (:)
$\kappa_i$	Planck mean absorption coefficient for species $i$ (1/(m*Pa))
$\mu$	dynamic viscosity (kg/(m*s))
$\mu_i$	dynamic viscosity of species $i$ (kg/(m*s))
$\rho$	gas density (kg/m <sup>3</sup> )
$\sigma_B$	Boltzmann constant ((m <sup>2</sup> *kg)/(s <sup>2</sup> *K))
$\sigma_{i,n}$	site occupancy number of species $i$ at site $n$ (:)
$\omega_i$	species production rate from reactions in given phase, (mole/m <sup>3</sup> ) for gas phase, (mole/m <sup>2</sup> ) for surface phase

**Subscripts**

$g$	Bulk gas
$in$	Inlet flow to the cell
$i$	Species $i$
$j$	Species $j$
$l$	Current washcoat layer
$p$	Thin-film layer gas
$s$	Substrate material
$x-$	Negative horizontal direction
$x+$	Positive horizontal direction
$y-$	Negative vertical direction
$y+$	Positive vertical direction

**Abbreviations**

GHSV	Gas hourly space velocity
MGT	Micro gas turbine
MSR	Methane steam reforming
SOFC	Solid oxide fuel cell

**References**

1. Yusaf, T.; Fernandes, L.; Abu Talib, A.; Altarazi, Y.; Alrefae, W.; Kadirgama, K.; Ramasamy, D.; Jayasuriya, A.; Brown, G.; Mamat, R.; et al. Sustainable Aviation—Hydrogen Is the Future. *Sustainability* **2022**, *14*, 548. [[CrossRef](#)]
2. Jain, I. Hydrogen the fuel for 21st century. *Int. J. Hydrogen Energy* **2009**, *34*, 7368–7378. [[CrossRef](#)]
3. Zuben, T.; Moreira, D.; Germscheidt, R.; Yoshimura, R.; Dorretto, D.; Araujo, A.; Salles, A., Jr.; Bonacin, J. Is hydrogen indispensable for a sustainable world? A review of H<sub>2</sub> applications and perspectives for the next years. *J. Braz. Chem. Soc.* **2022**, *33*, 824–843. [[CrossRef](#)]
4. European Commission. *The European Green Deal*; European Commission: Brussels, Belgium, 2019; Volume 53, p. 24.
5. Cuevas, F.; Zhang, J.; Latroche, M. The vision of France, Germany, and the European Union on future hydrogen energy research and innovation. *Engineering* **2021**, *7*, 715–718. [[CrossRef](#)]
6. Felseghi, R.; Carcadea, E.; Raboaca, M.; Trufin, C.; Filote, C. Hydrogen fuel cell technology for the sustainable future of stationary applications. *Energies* **2019**, *12*, 4593. [[CrossRef](#)]
7. Mekhilef, S.; Saidur, R.; Safari, A. Comparative study of different fuel cell technologies. *Renew. Sustain. Energy Rev.* **2021**, *16*, 981–989. [[CrossRef](#)]
8. Berg, H.; Himmelberg, A.; Lehmann, M.; Dückerhoff, R.; Neumann, M. The Turbo-Fuel-Cell 1.0–family concept. *IOP Conf. Ser. Mater. Sci. Eng.* **2018**, *297*, 012004. [[CrossRef](#)]
9. Herrera Delgado, K. *Surface Reaction Kinetics for Oxidation and Reforming of H<sub>2</sub>, CO, and CH<sub>4</sub> over Nickel-Based Catalysts*; Karlsruher Institut für Technologie (KIT): Karlsruhe, Germany, 2014.
10. Younas, M.; Shafique, S.; Hafeez, A.; Javed, F.; Rehman, F. An overview of hydrogen production: Current status, potential, and challenges. *Fuel* **2022**, *316*, 123317. [[CrossRef](#)]
11. Rostrup-Nielsen, J. Production of synthesis gas. *Catal. Today* **1993**, *18*, 305–324. [[CrossRef](#)]
12. Angeli, S.; Monteleone, G.; Giaconia, A.; Lemonidou, A. State-of-the-art catalysts for CH<sub>4</sub> steam reforming at low temperature. *Int. J. Hydrogen Energy* **2014**, *39*, 1979–1997. [[CrossRef](#)]
13. Meloni, E.; Martino, M.; Palma, V. A short review on Ni based catalysts and related engineering issues for methane steam reforming. *Catalysts* **2020**, *10*, 352. [[CrossRef](#)]
14. Sá, S.; Silva, H.; Brandão, L.; Sousa, J.; Mendes, A. Catalysts for methanol steam reforming—A review. *Appl. Catal. Environ.* **2010**, *99*, 43–57. [[CrossRef](#)]
15. Rostrup-Nielsen, J. Coking on nickel catalysts for steam reforming of hydrocarbons. *J. Catal.* **1974**, *33*, 184–201. [[CrossRef](#)]

16. Pashchenko, D.; Makarov, I. Carbon deposition in steam methane reforming over a Ni-based catalyst: Experimental and thermodynamic analysis. *Energy* **2021**, *222*, 119993. [[CrossRef](#)]
17. Trimm, D. Coke formation and minimisation during steam reforming reactions. *Catal. Today* **1997**, *37*, 233–238. [[CrossRef](#)]
18. Laidler, K.; Meiser, J. *Physical Chemistry*; Benjamin-Cummings Publishing Co., Subs. of Addison Wesley Longman, University of Michigan: Ann Arbor, MI, USA, 1982; Volume 1.
19. Baxter, R.; Hu, P. Insight into why the Langmuir–Hinshelwood mechanism is generally preferred. *J. Chem. Phys.* **2002**, *116*, 4379–4381. [[CrossRef](#)]
20. Bowen, J.; Acrivos, A.; Oppenheim, A. Singular perturbation refinement to quasi-steady state approximation in chemical kinetics. *Chem. Eng. Sci.* **1963**, *18*, 177–188. [[CrossRef](#)]
21. Saliccioli, M.; Stamatakis, M.; Caratzoulas, S.; Vlachos, D. A review of multiscale modeling of metal-catalyzed reactions: Mechanism development for complexity and emergent behavior. *Chem. Eng. Sci.* **2011**, *66*, 4319–4355. [[CrossRef](#)]
22. Quirino, P.; Amaral, A.; Pontes, K.; Rossi, F.; Manenti, F. Impact of kinetic models in the prediction accuracy of an industrial steam methane reforming unit. *Comput. Chem. Eng.* **2021**, *152*, 107379. [[CrossRef](#)]
23. Singh, C.; Saraf, D. Simulation of side fired steam-hydrocarbon reformers. *Ind. Eng. Chem. Process. Des. Dev.* **1979**, *18*, 1–7. [[CrossRef](#)]
24. Hou, K.; Hughes, R. The kinetics of methane steam reforming over a Ni/ $\alpha$ -Al<sub>2</sub>O catalyst. *Chem. Eng. J.* **2001**, *82*, 311–328. [[CrossRef](#)]
25. Numaguchi, T.; Kikuchi, K. Intrinsic kinetics and design simulation in a complex reaction network; steam-methane reforming. *Chem. Eng. Sci.* **1988**, *43*, 2295–2301. [[CrossRef](#)]
26. Xu, J.; Froment, G. Methane steam reforming, methanation and water-gas shift: I. Intrinsic kinetics. *AIChE J.* **1989**, *35*, 88–96. [[CrossRef](#)]
27. Maier, L.; Schädel, B.; Herrera Delgado, K.; Tischer, S.; Deutschmann, O. Steam reforming of methane over nickel: Development of a multi-step surface reaction mechanism. *Top. Catal.* **2011**, *54*, 845–858. [[CrossRef](#)]
28. Matera, S.; Schneider, W.; Heyden, A.; Savara, A. Progress in accurate chemical kinetic modeling, simulations, and parameter estimation for heterogeneous catalysis. *ACS Catal.* **2019**, *9*, 6624–6647. [[CrossRef](#)]
29. Loge AB©. 2022. Available online: <http://logesoft.com/logesoft-ware/> (accessed on 3 March 2022).
30. Fröjd, K.; Mauss, F. A three-parameter transient 1D catalyst model. *SAE Int. J. Engines* **2011**, *4*, 1747–1763. [[CrossRef](#)]
31. Aslanjan, J.; Klauer, C.; Perlman, C.; Günther, V.; Mauss, F. *Simulation of a Three-Way Catalyst Using Transient Single and Multi-Channel Models*; SAE Technical Paper; SAE: Detroit, MI, USA, 2017.
32. Richter, J.; Günther, V.; Mauss, F. Reaction mechanism development and investigation on the convergence influence in a 1D catalyst model for a  $\gamma$ -alumina stabilized three-way catalyst. In Proceedings of the International Symposium on Diagnostics and Modeling of Combustion in Internal Combustion Engines, Sapporo, Japan, 28–31 July 2022; p. A10-3.
33. Rakhi, G.V.; Richter, J.; Mauss, F. Steam reforming of methane over nickel catalyst using a one-dimensional model. *Int. J. Environ. Sci.* **2022**, *5*, 1–32. [[CrossRef](#)]
34. Seidel, L. *Development and Reduction of a Multicomponent Reference Fuel for Gasoline*; BTU Cottbus-Senftenberg: Cottbus, Germany, 2017.
35. Incropera, F.; DeWitt, D.; Bergman, T.; Lavine, A. *Fundamentals of Heat and Mass Transfer 6E*; Wiley: New York, NY, USA, 2006.
36. Ramanathan, K.; Balakotaiah, V.; West, D. Light-off criterion and transient analysis of catalytic monoliths. *Chem. Eng. Sci.* **2003**, *58*, 1381–1405. [[CrossRef](#)]
37. Santos, H.; Costa, M. Modelling transport phenomena and chemical reactions in automotive three-way catalytic converters. *Chem. Eng. J.* **2009**, *148*, 173–183. [[CrossRef](#)]
38. DETCHEM Detailed Chemistry in CFD | Simulate Reacting Flows. 2022. Available online: <https://www.detchem.com/mechanisms> (accessed on 3 March 2022).

**Disclaimer/Publisher’s Note:** The statements, opinions and data contained in all publications are solely those of the individual author(s) and contributor(s) and not of MDPI and/or the editor(s). MDPI and/or the editor(s) disclaim responsibility for any injury to people or property resulting from any ideas, methods, instructions or products referred to in the content.